# Journal of Materials Chemistry A

Accepted Manuscript



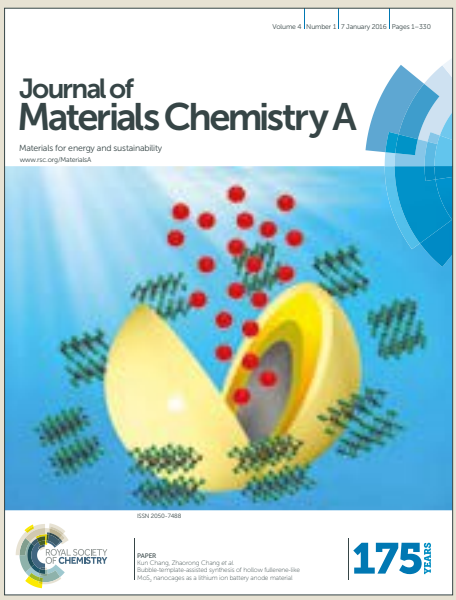




ROYAL SOCIETY OF CHEMISTRY

rsc.li/materials-a

View Article Online
DOI: 10.1039/C8TA02767F

Journal of Materials Chemistry A

ARTICLE

# A $CO_2$ Optical Sensor based on Self-Assembled Metal-Organic Framework Nanoparticles

Received 00th January 20xx,
Accepted 00th January 20xx

DOI: 10.1039/x0xx00000x

www.rsc.org/

Blanca Chocarro-Ruiz,[a] Javier Pérez-Carvajal,[a] Civan Avci,[a] Olalla Calvo-Lozano,[a] Maria Isabel Alonso,[b] Daniel Maspoch,*[ac] and Laura M. Lechuga*[ad]

The development of devices for sensing and monitoring $CO_2$ levels is crucial for many fields such as food packaging and for human safety indoors. Herein the fabrication of an optical $CO_2$ sensor by integration of a metal-organic framework (MOF) onto bimodal optical waveguides is reported. This sensor is constructed via self-assembly of a transparent film of zeolitic imidazolate framework-8 (ZIF-8) nanoparticles (size: 32 ± 5 nm) on the waveguides. The nanoZIF-8-based sensor exhibits a broad linear response, with limit of detections of 3130 ppm at room temperature and 774 ppm at 278 K. Furthermore, it is robust, selective, fast and reusable, and can be stored under humid conditions with no loss in performance.

## Introduction

Carbon dioxide is a known pollutant that affects the performance of humans in workplaces, schools and other indoor areas. High levels of ambient $CO_2$ can lead to tremors and loss of consciousness (>100000 ppm, 10%), and even to death (>250000 ppm, 25%).[1] However, indoors, the pernicious effects of $CO_2$ begin to appear at much lower levels. For example, $CO_2$ levels of 2,000 ppm to 5,000 ppm (0.2% to 0.5%) lead to headaches, sleepiness, elevated heart rate and diminished concentration, among other negative effects. Organizations such as the Occupational Safety and Health Administration (OSHA), Association Advancing Occupational and Environmental Health (ACGIH) and The National Institute for Occupational Safety and Health (NIOSH) have established $CO_2$ limits of 0.5% (8-hour time-weight average), 3%, (short-term exposure) and 4% (maximum instantaneous limit considered immediately dangerous to life and health).[2] To date, the most common devices on the market for $CO_2$ detection are non-dispersive infrared and electrochemical sensors. However, they still show some drawbacks including water interferences for the first type of sensors and short lifespan for the second ones.[3] Therefore, devices for sensing and monitoring indoor $CO_2$ levels are still urgently needed to ensure the safety of human occupants. Moreover, monitoring of $CO_2$ is important in many other fields such as food packaging, in which high $CO_2$ levels (10% to 80%) are used to suppress microbial growth.[4]

Interferometric waveguide devices are among the most sensitive sensors. They have myriad applications in areas such as environmental monitoring, medical diagnostics and food-safety analysis.[5] These devices are based on the detection of extremely small refractive index (RI) changes occurring on the sensor surface.[6] In them, a receptor layer -which is typically comprised of a selective biomolecule- is immobilized onto the waveguide surface.[7] When this bioreceptor recognizes and then interacts with the target analyte, a local shift of the RI occurs, which affects the properties of the light propagating through its evanescent wave (EW). This variation can be detected and subsequently correlated with the analyte concentration. Based on this principle, we previously developed a highly sensitive sensor device, which we call a bimodal waveguide (BiMW) interferometer (Figure 1a). BiMW sensors have a simple design characterized by a straight waveguide that obviates Y-type dividers or other, more complex structures that are difficult to manufacture, such as those found in conventional Mach-Zehnder or Young interferometers. They are also highly amenable to miniaturization and are compatible with microfluidics and well-known read-out techniques. Moreover, compared to classical EW sensors, BiMW sensors exhibit higher sensitivity for label-free and unamplified detection, with a limit of detection (LOD) close to 1 x $10^{-8}$ refractive index units (RIU).[8]

Metal-organic frameworks (MOFs) are a class of porous materials built from metal nodes coordinated to organic ligands.[9,10] Their unique chemical versatility and structure confer them with outstanding porosity[11] for countless potential applications, including gas storage, gas separation and catalysis.[12] Among these R&D areas, sensing is especially

[a] Catalan Institute of Nanoscience and Nanotechnology (ICN2), CSIC and BIST, Campus UAB, Bellaterra, 08193 Barcelona, Spain. *E-mail: daniel.maspoch@icn2.cat; laura.lechuga@icn2.cat
[b] Institut de Ciència de Materials de Barcelona (ICMAB-CSIC), Campus UAB, Bellaterra, 08193, Spain
[c] ICREA, Pg. Lluís Companys 23, Barcelona, 08010, Spain
[d] CIBER-BBN

Electronic Supplementary Information (ESI) available: [XRPD, FE-SEM images and UV-Vis spectroscopic characterization of the synthesized ZIF-8 particles, $CO_2$ sensor response optimization, optical images, FESEM images of the BiMW sensors, and $N_2$ and $CO_2$ adsorption isotherms]. See DOI: 10.1039/x0xx00000x

View Article Online
DOI: 10.1039/C8TA02767F



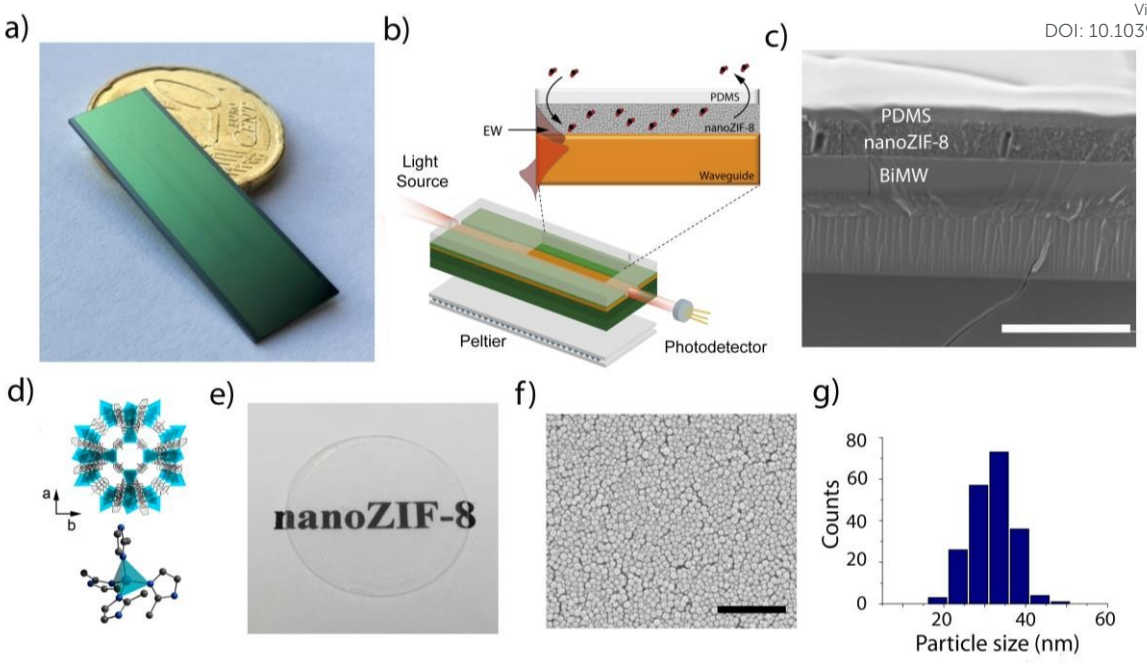


**Figure 1.** a) Photo of a chip containing 20 BiMW sensors. b) Schematic of the nanoZIF-8-based BiMW sensor. c) FE-SEM image (side view) of the nanoZIF-8-based BiMW sensor, showing the layers of nanoZIF-8 and PDMS built on top of the waveguide. Scale bar: 5 μm. d) Representation of the structure of ZIF-8. e) Photo of the transparent film of self-assembled ZIF-8 nanoparticles. f) Representative FE-SEM images of a self-assembled nanoZIF-8 film. Scale bar: 500 nm. g) Size-distribution histogram of the ZIF-8 nanoparticles (32 nm ± 5 nm).

prominent, owing to the high porosity of MOFs as well as to their sorption selectivity.[13] Reported advances in MOF-based sensors include integration of MOFs into mechanical (*e.g.* quartz crystal microbalances [QCMs],[14] microcantilevers,[15] surface acoustic waves [SAWs][16] and microresonators[17]), electrochemical and optical transducers,[18] all of which convert a chemical response into a read-out signal.[19] However, most of these approaches have been employed for detecting vapours, rather than gases. For gases, Eddaoudi *et al.* successfully developed a capacitive IDE sensor for $H_2S$ detection,[20] whereas Mirica *et al.* reported the fabrication of an electric sensor for NO detection.[21] For $CO_2$, Van Duyne *et al.* fabricated a Localized Surface Plasmon Resonance (LSPR) sensor with an HKUST-1 film that was able to detect ambient $CO_2$ levels down to 10%.[22] More recently, Wang *et al.* designed a near-IR fiber-optic coated with HKUST-1 that showed a LOD of 20 ppm for $CO_2$.[23] However, practical use of these MOF-based sensors for $CO_2$ detection is limited by the low hydrolytic stability of HKUST-1 and/or by scattering and water interferences. Herein, we report the adaptation of BiMW nanointerferometers for $CO_2$ sensing, based on integration of MOFs (as the selective receptor layer) onto a $Si_3N_4$ waveguide surface (Figure 1b,c). Zeolitic imidazole framework-8 (ZIF-8), a porous sodalite-type MOF made of Zn(II) ions and 2-methylimidazolate linkers (Figure 1d),[24] was selected because it exhibits a good thermal stability and a large surface area (≈ 1200 $m^2\ g^{-1}$ to 1500 $m^2\ g^{-1}$). It is also stable under high relative-humidity conditions, and is suitable for gas separation, since it is selective for $CO_2$ and $H_2$ over $N_2$, $O_2$ or $CH_4$.[25]

## Experimental

### Reagents

All chemical reagents and solvents were purchased from Sigma Aldrich and used as received without further purification. Milli-Q water from Millipore (USA) was always employed.

### Synthesis of nanoZIF-8 (size = 32 ± 5 nm)

The synthesis of the colloidal solution followed a slightly modified protocol previously reported by Cravillon *et al.*[26] $Zn(NO_3)_2{\cdot}6H_2O$ (1.47 g, 4.94 mmol) dissolved in 100 mL of methanol was added into 2-methylimidazole (3.24 g, 39.46 mmol) dissolved in 100 mL of methanol. The resulting mixture was then gently stirred for a few seconds at room temperature. Note that this mixture turned turbid after some seconds. After 7 min, the nanoparticles were separated from the dispersion by centrifugation at 11000 rpm for 10 min in 50 mL Falcon tubes. The pellets were then re-dispersed in 5 mL of methanol and centrifuged in 4 Eppendorf tubes at 18000 rpm for 15 min. The nanoZIF-8 particles were washed again with 2 mL of methanol and centrifuged in 2 Eppendorf tubes at 18000 rpm for 15 min (Figure S1†). The collected wet pellets were finally resuspended at a concentration of 100 mg/mL in Milli-Q water with cetyl trimethylammonium bromide (CTAB) dissolved. Note that the particles should be dispersed while they are still wet to prevent aggregation.

View Article Online
DOI: 10.1039/C8TA02767F





**Synthesis of nanoZIF-8 (size = 53 ± 8 nm)**

$Zn(NO_3)_2{\cdot}6H_2O$ (2.00 g, 6.72 mmol) dissolved in 100 mL of methanol was added into 2-methylimidazole (3.24 g, 39.46 mmol) dissolved in 100 mL of methanol. The resulting mixture was gentle stirred for a few seconds at room temperature. Note that the mixture turned turbid after several seconds. After 2 h, the nanoparticles were separated from the dispersion by centrifugation at 11000 rpm for 10 min in 50 mL Falcon tubes. The pellets were then redispersed in 5 mL of methanol and centrifuged in 4 Eppendorf tubes at 18000 rpm for 15 min. The nanoZIF-8 particles were washed again with 2 mL of methanol and centrifuged in 2 Eppendorf tubes at 18000 rpm for 15 min (Figure S1†). The collected wet pellets were finally resuspended at a concentration of 100 mg/mL in Milli-Q water with CTAB dissolved. Note that the particles should be dispersed while they are still wet to prevent aggregation.

**Synthesis of nanoZIF-8 (size = 70 ± 12 nm)**

$Zn(NO_3)_2{\cdot}6H_2O$ (3.00 g, 10.08 mmol) dissolved in 100 mL of methanol was added into 2-methylimidazole (6.00 g, 73.08 mmol) dissolved in 100 mL of methanol. The resulting mixture was gentle stirred for a few seconds at room temperature. Note that this mixture turned turbid after several seconds. After 2 h, the nanoparticles were separated from the dispersion by centrifugation at 11000 rpm for 10 min in 50 mL Falcon tubes. The pellets were then redispersed in 5 mL of methanol and centrifuged in 4 Eppendorf tubes at 18000 rpm for 15 min. The nanoZIF-8 particles were washed again with 2 mL of methanol and centrifuged in 2 Eppendorf tubes at 18000 rpm for 15 min (Figure S1†). The collected wet pellets were finally resuspended at a concentration of 100 mg/mL in Milli-Q water with CTAB dissolved. Note that the particles should be dispersed while they are still wet to prevent aggregation.

**NanoZIF-8 film formation and optimization**

First, the chips were cleaned/recycled by sequentially rinse with acetone, ethanol and water, followed by sonication in MeOH/HCl 1:1 (v/v) for 10 min, rinsing with water and dried with a stream of pure nitrogen. Then, a high optical quality nanoZIF-8 film was prepared using the spin-coating technique with a Laurell WS-650-23 spin coater (Laurell Technologies, PA, USA). To this end, the colloidal solution of nanoZIF-8 was spin-coated with an acceleration of 250 revolutions per minute (rpm) $s^{-1}$ and 1 min at room temperature under ambient atmospheric conditions. For the optimal film thickness, different concentrations and spinning speeds were evaluated. First, 200 µL from 10 mg $mL^{-1}$ to 120 mg $mL^{-1}$ of the nanoZIF-8 were deposited in each chip and then rotated at a spinning speed of 2000 rpm. The optimal film thickness was evaluated measuring the sensor response of 100 % $CO_2$ for each chip (Figure S2†). The highest signal response was achieved for 60 mg $mL^{-1}$. With that concentration, films were prepared at different spinning speeds from 2000 rpm to 6000 rpm. The highest signal response was achieved for 2000 rpm, which corresponds a film thickness of 1.15 µm ± 0.05 µm (evaluated with transversal cross-section of FE-SEM images).

**PDMS film formation**

PDMS pre-polymer and curing agent (SYLGARD 184 Silicone Elastomer Kit, Dow Corning, USA) were thoroughly mixed in a 10:1 weight ratio. A stock solution of 20 % (w/w) PDMS was prepared by dissolving the elastomer in toluene and stirred for 12 h. 200 µL of PDMS solution was deposited on top of the nanoZIF-8 film or directly onto the BiMW sensor, and then rotated at a spinning speed of 5000 rpm and an acceleration of 250 rpm $s^{-1}$ for 1 min. The coated films were subsequently cured in a hot-plate at 110 °C for 12 h.

**BiMW gas sensor performance**

The optical bimodal waveguide sensor and experimental set-up were fabricated as previously described.[8] In this device, changes in the RI in the vicinity of the sensor surface occur when $CO_2$ molecules interact with the porous nanoZIF-8 layer. The working principle of the BiMW sensor is based in the interference pattern generated by the superposition of only two light modes. The device is designed in such a way that a single mode is generated after the light is coupled in a straight rib waveguide and after passing through a step-junction, two transversal modes (fundamental and first order, respectively) with the same polarization are excited (see Fig. 1b). On the top cladding of the bimodal waveguide we define an open sensing window in order to have access to the waveguide surface. Any change occurring in the RI over the sensing area differently affect the effective refractive index (N) of the fundamental ($TE_{00}$) and the first order ($TE_{10}$) modes through their respective evanescent fields, producing a phase change (ΔΦ):

$$\Delta\Phi = \frac{2\pi L_{SA}}{\lambda(\Delta N_{TE10} - \Delta N_{TE00})}$$

where $L_{SA}$ is the length of the sensing area and λ is the working wavelength. The phase variation (ΔΦ) of the interference pattern caused by this shift generates a modification of the light output intensity distribution, captured by a two-section photodetector with an upper and lower section to generate $I_{up}$ and $I_{down}$ currents, respectively. The quantification of the sensor response can be evaluated by the change on this distribution, calculated by the normalized signal (*S*), according to the expression:

$$S = \frac{I_{up} - I_{down}}{I_{up} + I_{down}} \alpha \cos[\Delta\Phi(t)]$$

Each measurement of the sensor signal response (%) is represented in π rad phase variation (corresponding to a half oscillation or fringe of the interferometric sensor).

In the experimental set-up, a TE polarised light is coupled into the BiMW sensor by end-fire coupling method of a λ=660 nm and P=120 mW diode laser (ML101J27, Mitsubishi). A lenses system composed by collimated lens (C240TME-D, Thorlabs), polarization-dependent isolator (IO-3D-660-VLP, Thorlabs) and a coupling objective 40x (Achro, Leica) are used. Finally, for collecting the light at the end of the device, a four quadrants photodetector (S4349, Hamamatsu) is employed. For the real time signal acquisition, a home-made LabVIEW software (National Instruments, USA) is used. A stainless-steel gas cell with an o-ring is interfaced with the BiMW sensor to inject the

gas during experiments to the sensing windows isolated from the air. Different flow rates are delivered using 3 different Mass Flow Controllers (10 mLn or 0.7mLn EL-FLOW Bronkhorst® (MFC) for each gas ($N_2$ and $CO_2$) and pass through a static mixer to allow the homogeneous injection of $CO_2$ gas in dry $N_2$ flowed at atmospheric pressure. The BiMW sensor holder also incorporates a temperature controller providing temperature stabilization with an accuracy of 0.01 degrees. At the exit there is a Back-Pressure controller (0.2-1100 mbar, Bronkhorst®) (BKP) to control the pressure of the gas cell and a Pfeiffer DUO vacuum pump.

### Gas dosing

Utra-high purity grade $N_2$, $CO_2$ and $CH_4$ (Praxiar Premium were used for all experiments. All measurements were performed in triplicate and prior to each triplicate measurement the gas cell was left under vacuum and/or then purged with $N_2$ flux. The flow rates were regulated with the MFCs (of 10 mLn $min^{-1}$ or 0.7 mLn $min^{-1}$) allowing 1, 2 or 3 gases for each measurement and homogenously mixed with the static mixer before being dosed. After passing through the gas cell, the gas stream was diverted to the BKP and vacuum pump or to separate exhaust lines using direct-acting solenoid valves.

### Characterization

X-ray powder diffraction (XRPD) patterns of ZIF-8 samples were collected on an X'Pert PRO MPDP analytical diffractometer (Panalytical) at 45 kV, 40 mA using Cu Kα radiation (λ = 1.5419 Å), whereas XRD patterns of the ZIF-8 films were collected on an X'Pert PRO MRD analytical diffractometer (Panalytical) equipped with a parabolic mirror at 45 kV, 40 mA using Cu Kα radiation (λ = 1.5419 Å). FE-SEM images were collected on a FEI Magellan 400L scanning electron microscope at an acceleration voltage of 2.0 kV and FEI Quanta 650F scanning electron microscope with EDX Inca 250 SSD XMax20, using aluminum as support. The size of nanoZIF-8 particles was calculated from FE-SEM images by averaging the size of 200 particles measured using ImageJ software from images of different areas of the same samples. Volumetric $N_2$ and $CO_2$ sorption isotherm was collected at 77 K, 278K and 293K respectively using an AutosorbIQ-AG analyzer (Quantachrome Instruments) after outgassing the powder at 85 ºC under primary vacuum. Vis absorption spectra were recorded on a Cary 4000 UV-Vis spectrophotometer (Agilent Technologies, Santa Clara, CA, USA) using the nanoZIF-8 films deposited on glass substrates. The thickness of the different films was characterized with the transversal cross-section of FE-SEM images.

## Results and discussion

The first step in fabricating the MOF-BiMW sensor was the integration of ZIF-8 crystals onto the waveguide surface. Integration of ZIF-8 onto the surface of the BiMW waveguides was not straightforward, as most MOFs -including ZIF-8 itself- exhibit high optical absorption and/or scattering, consequently inhibiting light propagation.[23] To solve this problem, ZIF-8 was integrated on top of the waveguides in the form of transparent

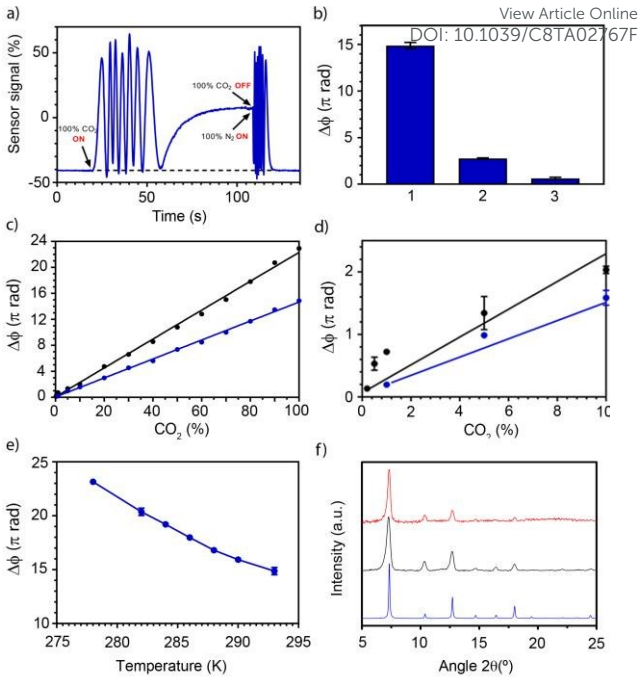


**Figure 2.** a) Real-time response signal to the change from pure $N_2$ flow to pure $CO_2$ flow. b) Responses to 100% $CO_2$ of the nanoZIF-8-based BiMW sensor (1), the BiMW sensor containing only the PDMS film (2), and the bare BiMW sensor (3). c,d) Calibration curves at 293 K (blue) and 278 K (black). e) Responses to 100% $CO_2$ of the nanoZIF-8-based BiMW sensor at different temperatures, from RT to 278 K. f) XRD patterns of the simulated ZIF-8 (blue), bare nanoZIF-8-based BiMW sensor (black) and after using it for the $CO_2$ detection experiments (red).

thin films (Figure 1e,f). These ZIF-8 films, whose transmittance at the BiMW operating wavelength (660 nm, Figure S1†) is greater than 90%, were fabricated by spin-coating deposition of aqueous colloidal solutions of CTAB-coated ZIF-8 nanoparticles (size: 32 ± 5 nm; hereafter named nanoZIF-8; Figure 1g).[27] Note that small nanoparticle size was crucial for fabricating the transparent films: indeed, use of larger particles (size: 53 nm ± 8 nm, or 70 nm ± 12 nm) produced translucent films with a transmittance (660 nm) of 70% (Figure S1†). In these films, scattering of the light hindered its transmission through the waveguide, thus precluding any sensing. In the transparent nanoZIF-8 films, light efficiently transmitted through the waveguide. Since the evanescent field of the transmitted light decays exponentially as it penetrates the outer medium (EW ≈ 300 nm), an optimum thickness for the nanoZIF-8 was sought (Figure S2†). Thus, the best performing film was 1.15 ± 0.05 µm thick (Figure 1c), as prepared by spin-coating (concentration: 60 mg nanoZIF-8 $mL^{-1}$; spinning speed: 2000 rpm; time: 1 min; acceleration: 250 rpm $s^{-1}$). This optimized value fits well into the EW penetration depth, thus enabling the maximum amount of nanoZIF-8 to sense $CO_2$.

Having coated the optimized nanoZIF-8 film onto the waveguide, we then protected it with a layer of polydimethylsiloxane (PDMS). This PDMS layer enabled permanent attachment of the nanoZIF-8 film onto the surface of the waveguide and prevented cracking of the film upon its activation (i.e. upon removal of the guest molecules in its



 

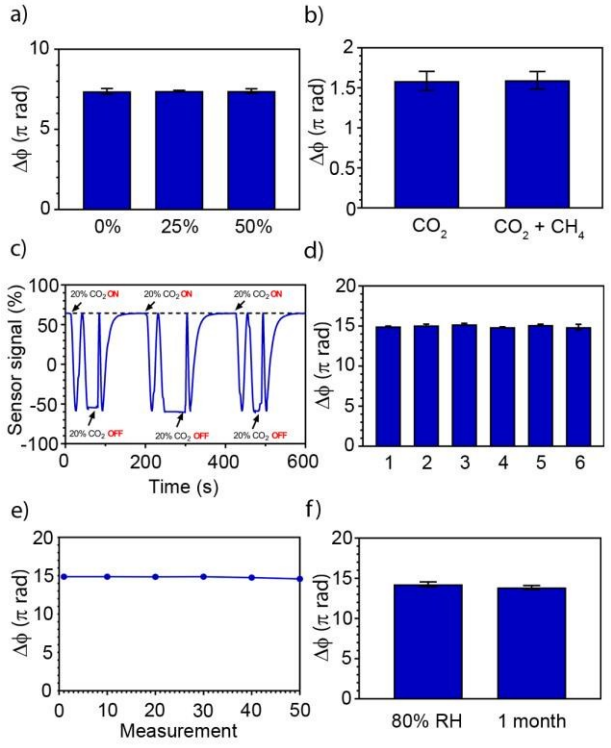


**Figure 3.** a) Sensor response to 50% $CO_2$ at relative humidity (RH) levels of 0%, 25% and 50%. b) Sensor response to 10% $CO_2$ in the presence and absence of 1% $CH_4$. c) Real-time detection cycles of three consecutive measurements of 20% $CO_2$. d) Response of six different sensors (1 to 3: different chips and same nanoZIF-8 batch; 4 to 6: same chip and different nanoZIF-8 batches) to 100% $CO_2$. e) 50 consecutive measurements at 100% $CO_2$. f) Sensor response to 100% $CO_2$ after storage under RH of 80% for 1 day or in the air for 1 month.

pores). This crack-prevention step was crucial, as in earlier experiments, exposure of nanoZIF-8 film under vacuum overnight at 60°C led to a complete loss of light transmission through the waveguide (Figure S3†). The rubbery polymer PDMS was chosen because is highly permeable to $CO_2$, enabling diffusion of $CO_2$ towards the nanoZIF-8 film.[28] Other polymers were tested, including poly(1-trimethylsilyl-1-propyne), which is also highly permeable to $CO_2$; however, the resulting films did not prevent cracking of the underlying nanoZIF-8 films—probably due to their glassy character.[29] To enhance the diffusivity of $CO_2$ through the PDMS layer, the thickness of the PDMS layer was minimized down to 0.66 ± 0.17 µm by spin-coating (spinning speed: 5000 rpm; time: 1 min; acceleration: 250 rpm $s^{-1}$) a solution of PDMS in toluene (concentration: 20% w/w) on the BiMW sensor. Then, the coated film was subsequently cured in a hot-plate at 110 °C for 12 h (Figure 1c).

As a final step, we activated the nanoZIF-8 on the BiMW sensor in-situ by heating it at 60 °C under vacuum overnight. This was done in the sensor set-up by equipping the exit with a vacuum pump and adding a Peltier element to the bottom of the platform for temperature control (Figures 1b, see also Figure S4†).

To evaluate our sensor's performance, we began by comparing the response for $CO_2$ detection of (1) the nanoZIF-8-based BiMW sensor with the respective responses obtained for (2) a bare BiMW sensor in the absence of nanoZIF-8 and PDMS, and (3) a BiMW sensor containing only the PDMS film (Figure S5†). To this end, the response of each sensor to a change from pure $N_2$ flow to pure $CO_2$ flow was evaluated at room temperature (RT, 293 K) (Figure 2a). From these experiments, we observed that in terms of signal amplification, the nanoZIF-8-based BiMW sensor was ~ 24-fold stronger than was the bare BiMW chip and ~ 4-fold stronger than the PDMS-based sensor (Figure 2b).

We then assessed the calibration and LOD of our nanoZIF-8-based BiMW sensor by analysing its performance under different concentrations of $CO_2$ established by variably mixing the $CO_2$ flow with the carrier $N_2$ flow at RT (Figure S6†). As shown in Figures 2c and d, the calibration curve shows a linear response in the range of 1% to 100% $CO_2$. The theoretical LOD was 3130 ppm of $CO_2$. Remarkably, this LOD could be lowered down to 774 ppm by simply decreasing the working temperature to 278 K. As shown in Figure 2e, the response of the sensor to a change from pure $N_2$ flow to pure $CO_2$ flow was amplified as the temperature decreased from RT to 278 K. This observation was consistent with previous reports that ZIF-8 exhibits greater $CO_2$ uptake and $CO_2$ selectivity (over $N_2$) at lower temperatures (Figure S7†).[30] Therefore, we repeated the same calibration experiment but decreased the temperature down to 278 K using the Peltier element. Under these conditions, we found a ~ 1.5-fold amplification of the $CO_2$ signal response at 100% $CO_2$ relative to that measured at RT (Figure 2c,d). At 278 K, the calibration curve showed a linear response in the range of 0.2% to 100% $CO_2$. It is also important to highlight here that XRD of the sensor after all these $CO_2$ measurements showed that nanoZIF-8 film retains its crystallinity (Figure 2f).

Having optimized integration of the nanoZIF-8 film and demonstrated the influence of temperature on $CO_2$-sensing, we then analysed the performance of our sensor device under humid conditions. Thus, the sensor was tested at a $CO_2$ concentration of 25% and a relative humidity (RH) of 25%, 50% and 75 %. It was also tested at a $CO_2$ concentration of 50% and a RH of 25% and 50%. Remarkably, its response in all cases was unaffected by the humidity (Figure 3a and Figure S8†), thus confirming that water does not interfere with the $CO_2$ detection and avoiding the need of a desiccation process.

Next, we characterized the sensor device in terms of selectivity, reusability, reproducibility and repeatability. First, we evaluated its selectivity for $CO_2$ over $N_2$ or $CH_4$, by measuring the sensor response from vacuum up to 1 bar of pressure for these three gases at RT. The selectivity reached up to 8:1 for $CO_2$ over $N_2$, and up to 3:1 for $CO_2$ over $CH_4$ (Figure S9†). For example, the sensing selectivity of the nanoZIF-8-based BiMW sensor was tested by measuring $CO_2$ in the presence of 1% $CH_4$; well above the 0.1% concentration recommended by NIOSH as the maximum concentration for an 8-hour work.[31] Under these conditions, the signal response was identical than in the absence of $CH_4$ (Figure 3b). A simple $N_2$ purge at RT was found to be sufficient to refresh the sensor for subsequent reuse (Figure 2a and 3c). Reproducibility was evaluated by fabricating distinct sensors using different BiMW chips and different

batches of nanoZIF-8 (Figure 3d). High reproducibility was observed, with a relative standard deviation of less than 2%. The repeatability of the sensor was assessed over more than 50 measurement-regeneration cycles, also with a signal reduction of less than 2% (Figure 3e). The low variability observed among the sensor chips and the nanoZIF-8 batches, and the high repeatability, are all vital indicators for future technology transfer endeavours with these sensors

Finally, we studied the stability of our sensors by storing them under high RH levels (80%) for 1 day, or in air for 1 month, then evaluating their responses to a change from pure $N_2$ flow to pure $CO_2$ flow at RT. For sensors stored under each condition, the corresponding responses were identical to those of freshly prepared ones (Figure 3f). We hypothesize that the high stability is due not only to the hydrolytic stability of ZIF-8 but also to the PDMS layer, which anchors the MOF nanoparticles and protects them from the environment.

## Conclusions

In summary, we have reported the fabrication of a BiMW sensor device for detecting $CO_2$, based on self-assembly of a transparent film of ZIF-8 nanoparticles on the surface of the BiMW waveguides. The sensor showed a broad linear response, with LODs of 3130 ppm at room temperature and 774 ppm at 278 K; values that are below the threshold for $CO_2$ monitoring in food packaging and for human safety indoors. Its $CO_2$ selectivity was confirmed in the presence of water vapour and $CH_4$. Furthermore, our sensor exhibited a repeatability with an RSD < 2% and a response time of only a few seconds. This sensor proved to be efficient for at least 50 measurements followed by regeneration cycles, and was stable after storage in either of two test conditions (1 month in air; or 1 day at 80% RH). Moreover, the sensor fabrication was highly reproducible when different chips and nanoZIF-8 batches were used. These properties pave the way for using MOFs to develop robust, cheap, stable and fast sensors for $CO_2$ detection. In addition, as the BiMW technology can be easily adapted to conform portable sensors,[32] our work should enable the development of fully integrated MOF-based sensors for *in-situ* gas sensing and other *in-situ* practical applications.

## Acknowledgements

This work was supported by a grant from the Fundación Domingo Martínez (Ayuda a la Investigación 2016. Área de Aplicaciones Materiales), the Spanish MINECO (projects PN MAT2015-65354-C2-1-R and MAT2016-79053-P), the Catalan AGAUR (project 2014 SGR 80 and 2014 SGR 624), and the ERC, under the EU FP7 (ERC-Co 615954). It was also funded by the CERCA Program/Generalitat de Catalunya. This work also made use of the Spanish ICTS Network MICRONANOFABS, which is partially supported by MEINCOM. ICN2 and ICMAB acknowledge the support of the Spanish MINECO through the Severo Ochoa Centers of Excellence Program, under Grants SEV-2013-0295 and SEV-2015-0496.

## Notes and references

View Article Online
DOI: 10.1039/C8TA02767F

1 U. Satish, M. J. Mendell, K. Shekhar, T. Hotchi, D. Sullivan, S. Streufert and W. J. Fisk, *Environ. Health Perspect.*, 2012, **120**, 1671–1677.
2 Chemical Sampling Information | Carbon Dioxide | Occupational Safety and Health Administration, https://www.osha.gov/dts/chemicalsampling/data/CH_225400.html, (accessed 15 January 2018).
3 R. Piedrahita, Y. Xiang, N. Masson, J. Ortega, A. Collier, Y. Jiang, K. Li, R. P. Dick, Q. Lv, M. Hannigan and L. Shang, *Atmos. Meas. Tech*, 2014, **7**, 3325–3336.
4 K. B. Biji, C. N. Ravishankar, C. O. Mohan and T. K. Srinaval Gopal, *J. Food Sci. Technol.*, 2015, **52**, 6125-6135; P. Puligundla, J. Jung and S. Ko, *Food Control*, 2012, **25**, 328-333.
5 F. S. Ligler, *Anal. Chem.*, 2009, **81**, 519–526; B. Chocarro-Ruiz, A. Fernández-Gavela, S. Herranz and L. M. Lechuga, *Curr. Opin. Biotechnol.*, 2017, **45**, 175–183.
6 M. C. Estevez, M. Alvarez and L. M. Lechuga, *Laser Photon. Rev.*, *2012*, **6**, 463–487.
7 P. Kozma, F. Kehl, E. Ehrentreich-Förster, C. Stamm and F. F. Bier, *Biosens. Bioelectron.*, 2014, **58**, 287–307.
8 K. E. Zinoviev, A. B. González-Guerrero, C. Domínguez and L. M. Lechuga, *J. Light. Technol.*, 2011, **29**, 1926–1930.
9 S. Kaskel, *The Chemistry of Metal-Organic Frameworks: Synthesis, Characterization, and Applications*, Wiley-VCH, Weinheim, 2016.
10 H. C. Zhou, J. R. Long and O. M. Yaghi, *Chem. Rev.*, 2012, **112**, 673–674.
11 H. Furukawa, N. Ko, Y. B. Go, N. Aratani, S. B. Choi, E. Choi, A. O. Yazaydin, R. Q. Snurr, M. O'Keeffe, J. Kim and O. M. Yaghi, *Science*, 2010, **329**, 424–428.
12 O. K. Farha, A. Özgür Yazaydın, I. Eryazici, C. D. Malliakas, B. G. Hauser, M. G. Kanatzidis, S. T. Nguyen, R. Q. Snurr and J. T. Hupp, *Nat. Chem.*, 2010, **2**, 944–948; J.-R. Li, R. J. Kuppler and H.-C. Zhou, *Chem. Soc. Rev.*, 2009, **38**, 1477; J. Gascon, A. Corma, F. Kapteijn and F. X. Llabrés I Xamena, *ACS Catal.*, 2014, **4**, 361–378.
13 L. E. Kreno, K. Leong, O. K. Farha, M. Allendorf, R. P. Van Duyne and J. T. Hupp, *Chem. Rev.*, 2012, **112**, 1105–1125.
14 R. Ameloot, L. Stappers, J. Fransaer, L. Alaerts, B. F. Sels and D. E. De Vos, *Chem. Mater.*, 2009, **21**, 2580–2582.
15 M. D. Allendorf, R. J. T. Houk, L. Andruszkiewicz, A. A. Talin, J. Pikarsky, A. Choudhury, K. A. Gall and P. J. Hesketh, *J. Am. Chem. Soc.*, 2008, **130**, 14404–14405.
16 A. L. Robinson, V. Stavila, T. R. Zeitler, M. I. White, S. M. Thornberg, J. A. Greathouse and M. D. Allendorf, *Anal. Chem.*, 2012, **84**, 7043–7051.
17 Y. Hwang, H. Sohn, A. Phan, O. M. Yaghi and R. N. Candler, *Nano Lett.*, 2013, **13**, 5271–5276.
18 M. G. Campbell and M. Dincă, *Sensors*, 2017, **17**, 1108; O. Dalstein, D. R. Ceratti, C. Boissière, D. Grosso, A. Cattoni and M. Faustini, *Adv. Funct. Mater.*, 2016, **26**, 81-90.
19 I. Stassen, N. Burtch, A. Talin, P. Falcaro, M. Allendorf and R. Ameloot, *Chem. Soc. Rev.*, 2017, **46**, 3185-3241.
20 O. Yassine, O. Shekhah, A. H. Assen, Y. Belmabkhout, K. N. Salama and M. Eddaoudi, *Angew. Chem. Int. Ed.*, 2016, **55**, 15879–15883.
21 M. K. Smith, K. E. Jensen, P. A. Pivak and K. A. Mirica, *Chem. Mater.*, 2016, **28**, 5264-5268.
22 L. E. Kreno, J. T. Hupp and R. P. Van Duyne, *Anal. Chem.*, 2010, **82**, 8042–8046.

View Article Online
DOI: 10.1039/C8TA02767F

23 X. Chong, K.-J. Kim, E. Li, Y. Zhang, P. R. Ohodnicki, C.-H. Chang and A. X. Wang, *Sensors Actuators B Chem.*, 2016, **232**, 43–51.
24 K. S. Park, Z. Ni, A. P. Côté, J. Y. Choi, R. Huang, F. J. Uribe-Romo, H.K. Chae, M. O'Keeffe and O. M. Yaghi, *Proc. Natl. Acad. Sci.*, 2006, **103**, 10186-10191.
25 B. Chen, Z. Yang, Y. Zhu and Y. Xia, *J. Mater. Chem. A*, 2014, **2**, 16811-16831.
26 J. Cravillon, S. Münzer, S. J. Lohmeier, A. Feldhoff, K. Huber and M. Wiebcke, *Chem. Mater.*, 2009, **21**, 1410–1412.
27 C. Avci, I. Imaz, A. Carné-Sánchez, J. A. Pariente, N. Tasios, J. Pérez-Carvajal, M. I. Alonso, A. Blanco, M. Dijkstra, C. López and D. Maspoch, *Nat. Chem.*, 2018, **10**, 78-84.
28 W. L. Robb, *Ann. N. Y. Acad. Sci.*, 1968, **146**, 119–137.
29 R. Srinivasan, S. R. Auvil and P. M. Burban, *J. Memb. Sci.*, 1994, **86**, 67–86.
30 H. Huang, W. Zhang, D. Liu, B. Liu, G. Chen and C. Zhong, *Chem. Eng. Sci.*, 2011, **66**, 6297–6305.
31 CDC - METHANE - International Chemical Safety Cards - NIOSH, https://www.cdc.gov/niosh/ipcsneng/neng0291.html, (accessed 15 January 2018).
32 D. Duval, A. B. González-Guerrero, S. Dante, J. Osmond, R. Monge, L. J. Fernández, K. E. Zinoviev, C. Domínguez and L. M. Lechuga, *Lab Chip*, 2012, **12**, 1987-1994.

View Article Online
DOI: 10.1039/C8TA02767F



**Table of contents**

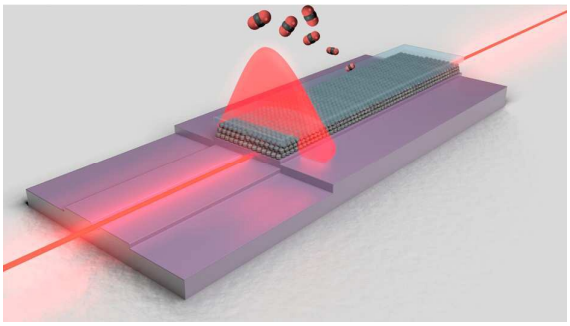

An optical $CO_2$ sensor is fabricated by integration of a self-assembled, transparent film of zeolitic imidazolate framework-8 (ZIF-8) nanoparticles onto bimodal optical waveguides. This sensor shows a limit of detection (LOD) of 774 ppm $CO_2$, is robust, fast and reusable, and can be stored under humid conditions with no loss in performance.